JOURNAL OF GUIDANCE, CONTROL, AND DYNAMICS
Vol. 21, No. 3, May–June 1998

Agile Missile Dynamics and Control

Kevin A. Wise* and David J. Broy†
The Boeing Company, St. Louis, Missouri 63166

The dynamics and technical challenges of controlling missiles capable of high-angle-of-attack flight are discussed. The missile control effectors discussed include thrust vectoring, reaction jet thrusters, and aerodynamic tail surfaces. A control power analysis is summarized that indicates the effectiveness of these control effectors over the missile's flight envelope. The six-degree-of-freedom dynamics for high-angle-of-attack missile flight control are presented. Autopilot design models and nonlinear simulation results demonstrating high-angle-of-attack flight are also presented.

Introduction

IN aircraft close-in-combat scenarios, a large off-boresight angle targeting capability, or the ability to engage targets in the rear hemisphere, is a significant advantage. Superagility in missiles refers to this capability. Following a successful missile launch and separation, dynamic pressures are often too low for aerodynamic controls to make a quick turn. When the propulsion system ignites, vectoring the thrust (or using reaction jets) can provide this capability, and as the velocity increases, the aerodynamic surfaces become more effective. For the missile to possess superagility (high-angle-of-attack capability) some form of alternate control is needed.

Figure 1 illustrates the maneuvering of an agile missile from launch to endgame, indicating a high-angle-of-attack (AOA) maneuvering capability provided by either thrust vector control (TVC) or reaction control system (RCS) thrusters. Some of the technological challenges for agile missile high-AOA flight include asymmetric vortex shedding, high-AOA stability variations, roll control, jet interaction effects, nonlinear blended autopilots, agile missile guidance, and fast-response propulsive controls and their integration with the main engine.

This paper discusses these challenges and the dynamics and flight control of agile missiles using alternate controls (TVC and/or RCS thrusters). A detailed presentation of the nonlinear dynamics is made. This derivation of the nonlinear equations and the resulting linearization to form autopilot design models are needed to illustrate how the dynamics at high AOAs differ from conventional low-AOA dynamics. The autopilot design models, actuator characteristics, and sensor models are presented, along with the flight control system simulation results from a high-fidelity nonlinear simulation.

Missile Dynamics

The body axis six-degree-of-freedom equations of motion[1,2] (EOM) are used in the design of the flight control system. Assuming a rigid body, constant mass, and inertia, the standard six-degree-of-freedom body EOM are written as

$$\begin{aligned}
\dot{u} &= rv - qw + X + G_x + T_x \\
\dot{v} &= pw - ru + Y + G_y + T_y \\
\dot{w} &= qu - pv + Z + G_z + T_z \\
\dot{p} &= -L_{pq}pq - L_{qr}qr + L + L_T \\
\dot{q} &= -M_{pr}pr - M_{r^2p^2}(r^2 - p^2) + M + M_T \\
\dot{r} &= -N_{pq}pq - N_{qr}qr + N + N_T
\end{aligned} \tag{1}$$

where G_i models gravity; X, Y, and Z model the linear accelerations produced by the aerodynamic forces; L, M, and N model the angular accelerations produced by the aerodynamic moments; T_x, T_y, and T_z model propulsion system forces; and L_T, M_T, and N_T model the moments produced by the propulsion system. Note that these variables have units of acceleration. The aerodynamic forces C_x, C_y, and C_z are modeled as nondimensional quantities and are scaled to units of force. This scaling is described by

$$\begin{bmatrix} X \\ Y \\ Z \end{bmatrix} = \frac{\bar{q}S}{m}\begin{bmatrix} C_x \\ C_y \\ C_z \end{bmatrix} \tag{2}$$

where $\bar{q}$ (lb/ft^2) is the dynamic pressure; S (ft^2) is a reference area; m is the mass in slugs; and C_x, C_y, and C_z are nondimensional aerodynamic forces. The aerodynamic moments acting on the body are similarly modeled as

$$\begin{bmatrix} L \\ M \\ N \end{bmatrix} = \begin{bmatrix} \dfrac{\bar{q}Sl}{I_{xx}I_{zz} - I_{xz}^2}(C_l I_{zz} + C_n I_{xz}) \\ \dfrac{\bar{q}Sl}{I_{yy}}C_m \\ \dfrac{\bar{q}Sl}{I_{xx}I_{zz} - I_{xz}^2}(C_n I_{xx} + C_l I_{xz}) \end{bmatrix} \tag{3}$$

where C_l, C_m, and C_n model nondimensional moments and l is a reference length. Note that the cross-axis inertia term I_{xz} couples the roll-yaw moment equations.

The gravitational forces are modeled as

$$\begin{bmatrix} G_x \\ G_y \\ G_z \end{bmatrix} = g\begin{bmatrix} -\sin(\theta) \\ \cos(\theta)\sin(\phi) \\ \cos(\theta)\cos(\phi) \end{bmatrix} \tag{4}$$

The pitch-plane angle-of-attack α and yaw-plane sideslip angle β are defined in Fig. 2, along with the total angle of attack α_T. The stability axis coordinates are a transformation of the body axes using α. The wind axis coordinates are a transformation from stability axes using β.

Aerodynamics

The missile's aerodynamic forces (C_x, C_y, and C_z) and moments (C_l, C_m, and C_n) are typically modeled as functions of α, β, Mach, body rates (p, q, and r), $\dot{\alpha}$, $\dot{\beta}$, the aerodynamic control surface deflections (δ_e, δ_a, and δ_r), center-of-gravity changes, and whether the main propulsion system is on or off and is referred to as plume effects. Also, the aerodynamic forces may depend upon whether reaction jets are on or off and is referred to as jet interaction effects. These complicated and highly nonlinear functions are used in the EOM to model the airframe's aerodynamics.

Asymmetric vortex shedding is a nonlinear phenomenon that must be addressed when considering high-AOA flight. Figure 3 illustrates the effect of asymmetric nose vortices at high AOAs with

---

Presented as Paper 96-3912 at the AIAA Guidance, Navigation, and Control Conference, San Diego, CA, July 29–31, 1996; received Jan. 21, 1997; revision received Oct. 31, 1997; accepted for publication Nov. 26, 1997.

*Senior Principal Technical Specialist, P.O. Box 516. Associate Fellow AIAA.

†Senior Project Engineer, P.O. Box 516.

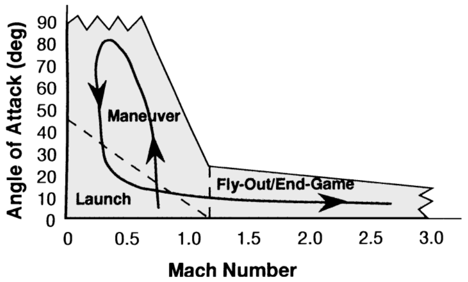

Fig. 1 Agile missile flight envelope.

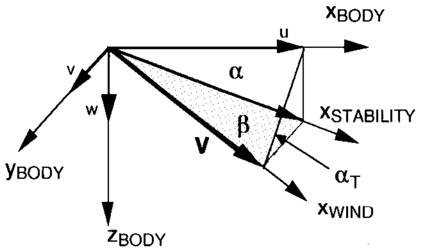

Fig. 2 Coordinate systems used in missile dynamics.

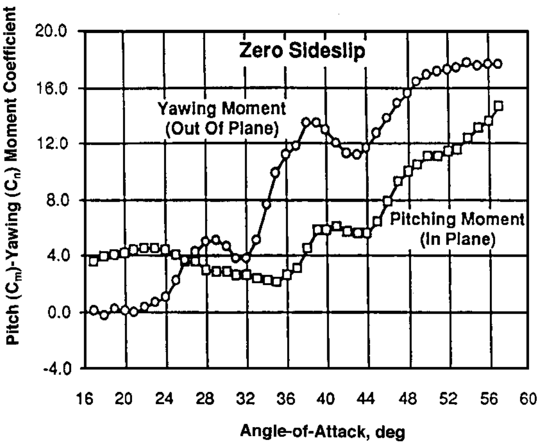

Fig. 3 Out-of-plane moment caused by asymmetric vortex shedding.

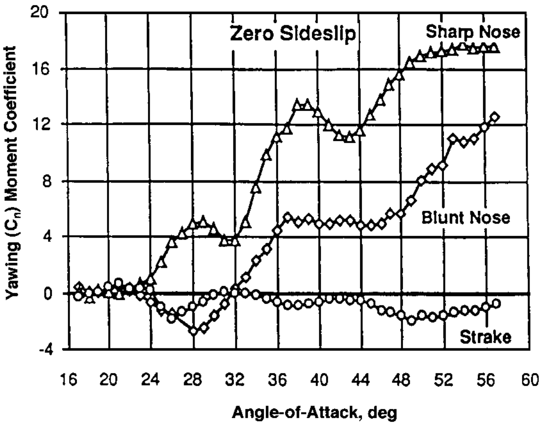

Fig. 4 Configuration redesign reduces asymmetric vortex shedding.

zero sideslip. Note that, due to the asymmetric vortices, the out-of-plane moment (yaw moment) is larger than the in-plane moment (pitch moment).

These asymmetric vortices can cause the nose to slice right or left and may require large control inputs to counter the effect. This phenomenon is often referred to as phantom yaw and can be mitigated by the addition of small nose strakes and/or nose bluntness. Figure 4 illustrates the possible reduction in out-of-plane moment by modifying the missile's configuration.

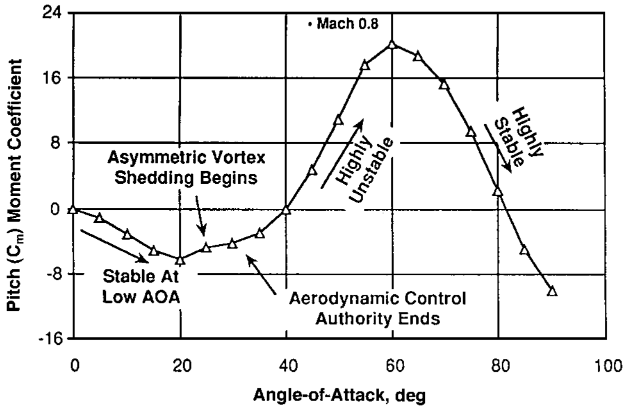

Fig. 5 Missile pitch-plane stability characteristics with angle of attack.

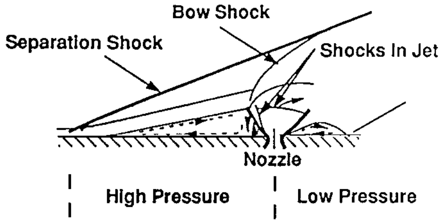

Fig. 6 Interaction of jet plume with freestream aerodynamics.

In addition to the challenge of overcoming phantom yaw, the missile's static stability significantly changes with AOA. Figure 5 illustrates the changing pitch plane stability with AOA. A positive slope is unstable, and a negative slope is stable. For the missile under investigation, aerodynamic control authority ends at or near 30-deg AOA, and some form of alternate control is needed to fly at high AOAs.

When RCS thrusters are used for control, there is an interaction of the jet plume with the freestream aerodynamic flow. Figure 6 illustrates this jet interaction, which is very nonlinear with AOA. Note the high- and low-pressure areas in front and back of the nozzle. This occurs when the jet plume is entrapped by the freestream flow. The entrapped high-pressure region (times its area and moment arm) produces a moment on the missile that is larger than the jet thrust force times its moment arm (distance to the c.g.). By exploiting this phenomenon, a smaller reaction jet can be used, thus reducing propellant requirements. This amplification, if not accounted for, would be an increase in the loop gain in the flight control system, which can significantly impact stability.

If the jet plume penetrates the freestream flow, the high-pressure field does not form, with the net thrust force produced by the jet reduced by the low-pressure field. Thus a 200-lb thruster may only produce 80 lb of thrust. This attenuation, if not accounted for, would be a decrease in the loop gain in the flight control system that can also impact stability for an open-loop unstable missile.

A key parameter in modeling the jet interaction phenomena is the jet penetration height. This parameter indicates if there is an amplification or an attenuation of the jet thrust (force). Unfortunately, this parameter varies significantly with flight condition and is difficult to predict. These nonlinear jet interaction effects also cause the moments produced by the thruster not to be proportional to the thruster force.

Propulsion System Forces and Moments

For TVC actuators,[3] the autopilot is designed to command the TVC actuator angle δ_T (rad). For the RCS thrusters, the autopilot is designed to command the thrust level T_{RCS} (lb).

The TVC forces and moments are modeled using a constant thrust that is deflected by the actuator. It is assumed that the actuator can deflect the thrust vector only in the pitch (δ_{T_e}) and yaw (δ_{T_r}) planes, using two actuators devoted to this task. (No roll control from the

TVC actuation system is assumed.) The resulting thrust [used in Eq. (1)] along the body axes is

$$\begin{bmatrix} T_x \\ T_y \\ T_z \end{bmatrix} = \frac{T}{m} \begin{bmatrix} \cos\left(\delta_{T_e}\right)\cos\left(\delta_{T_r}\right) \\ -\sin\left(\delta_{T_r}\right) \\ -\sin\left(\delta_{T_e}\right)\cos\left(\delta_{T_r}\right) \end{bmatrix} \tag{5}$$

where T is the axial thrust of the main propulsion system. The roll, pitch, and yaw moments (L_T, M_T, and N_T) produced by the TVC will be the moment arm $l_T = x_{\text{c.g.}} - x_{\text{TVC}}$ times the preceding pitch and yaw forces, respectively, and are described as

$$\begin{bmatrix} L_T \\ M_T \\ N_T \end{bmatrix} = \begin{bmatrix} \dfrac{-l_T I_{xz} T \sin\left(\delta_{T_r}\right)}{I_{xx} I_{zz} - I_{xz}^2} \\ \dfrac{l_T T \sin\left(\delta_{T_e}\right)\cos\left(\delta_{T_r}\right)}{I_{yy}} \\ \dfrac{-l_T I_{xx} T \sin\left(\delta_{T_r}\right)}{I_{xx} I_{zz} - I_{xz}^2} \end{bmatrix} \tag{6}$$

An RCS also produces propulsion forces and moments. The reaction jets are assumed to be positioned such that no axial force is generated. The RCS control system is designed to provide roll, pitch, and yaw moment control. The forces produced by the pitch and yaw jets are modeled as

$$\begin{bmatrix} 0 \\ T_y \\ T_z \end{bmatrix} = \frac{1}{m} \begin{bmatrix} 0 \\ \bar{T}_y \\ \bar{T}_z \end{bmatrix} \tag{7}$$

where $\bar{T}_y$ and $\bar{T}_z$ are the RCS thrust forces in the y-body (yaw) and z-body (pitch) directions, respectively. These moments produced by the thrusters are modeled by the x_{RCS} thruster forces multiplied by the moment arm $l_T = x_{\text{c.g.}} - x_{\text{RCS}}$. It is assumed here that the pitch and yaw jets are located at the same missile x station x_{RCS}.

Roll jets may also be used to control missile roll. These jets are symmetrically placed so that only a rolling moment is produced and is modeled as

$$L_T = \frac{l_{\text{Roll}} \bar{T}_{\text{Roll}}}{I_{xx}} \tag{8}$$

Adding this to the moments produced from the pitch and yaw jets results in

$$\begin{bmatrix} L_T \\ M_T \\ N_T \end{bmatrix} = \begin{bmatrix} \dfrac{l_{\text{Roll}} \bar{T}_{\text{Roll}}}{I_{xx}} + \dfrac{l_T I_{xz} \bar{T}_y}{I_{xx} I_{zz} - I_{xz}^2} \\ -\dfrac{l_T \bar{T}_z}{I_{yy}} \\ \dfrac{l_T I_{xx} \bar{T}_y}{I_{xx} I_{zz} - I_{xz}^2} \end{bmatrix} \tag{9}$$

Angle-of-Attack and Sideslip Dynamics

The following derivation will form a set of differential equations describing the dynamics for $\dot{V}$, $\dot{\alpha}$, and $\dot{\beta}$ valid for large α and $\beta < 90$ deg. Consider the following definition of the body velocities from Fig. 2:

$$u = V\cos(\alpha)\cos(\beta), \qquad v = V\sin(\beta)$$
$$w = V\sin(\alpha)\cos(\beta) \tag{10}$$

where V is the magnitude of the missile velocity vector. This can be represented as a transformation of the wind-axis velocity vector to the body axes as follows:

$$\begin{bmatrix} u \\ v \\ w \end{bmatrix}_{\text{BODY}} = S_\alpha S_\beta \begin{bmatrix} V \\ 0 \\ 0 \end{bmatrix}_{\text{WIND}} \tag{11}$$

where the transformations S_α and S_β are

$$S_\alpha = \begin{bmatrix} c\alpha & 0 & -s\alpha \\ 0 & 1 & 0 \\ s\alpha & 0 & c\alpha \end{bmatrix}, \qquad S_\beta = \begin{bmatrix} c\beta & -s\beta & 0 \\ s\beta & c\beta & 0 \\ 0 & 0 & 1 \end{bmatrix} \tag{12}$$

where $c(\cdot)$ and $s(\cdot)$ denote $\cos(\cdot)$ and $\sin(\cdot)$, respectively. Differentiating Eq. (11) yields

$$\begin{bmatrix} \dot{u} \\ \dot{v} \\ \dot{w} \end{bmatrix} = \begin{bmatrix} c\alpha c\beta & -s\alpha c\beta & -c\alpha s\beta \\ s\beta & 0 & c\beta \\ s\alpha c\beta & c\alpha c\beta & -s\alpha s\beta \end{bmatrix} \begin{bmatrix} \dot{V} \\ V\dot{\alpha} \\ V\dot{\beta} \end{bmatrix} \tag{13}$$

Inverting the coefficient matrix in the preceding equation yields

$$\begin{bmatrix} \dot{V} \\ V\dot{\alpha} \\ V\dot{\beta} \end{bmatrix} = \underbrace{\frac{-1}{c\beta} \begin{bmatrix} -c\alpha c^2\beta & -s\beta c\beta & -c^2\beta s\alpha \\ s\alpha & 0 & -c\alpha \\ s\beta c\beta c\alpha & -c^2\beta & s\alpha s\beta c\beta \end{bmatrix}}_{W(\alpha,\,\beta)} \begin{bmatrix} \dot{u} \\ \dot{v} \\ \dot{w} \end{bmatrix} \tag{14}$$

Substituting from Eq. (1) yields

$$\begin{bmatrix} \dot{V} \\ V\dot{\alpha} \\ V\dot{\beta} \end{bmatrix} = W(\alpha, \beta) \left(-\begin{bmatrix} p \\ q \\ r \end{bmatrix} \times \begin{bmatrix} u \\ v \\ w \end{bmatrix} + \begin{bmatrix} X \\ Y \\ Z \end{bmatrix} + \begin{bmatrix} G_x \\ G_y \\ G_z \end{bmatrix} + \begin{bmatrix} T_x \\ T_y \\ T_z \end{bmatrix} \right) \tag{15}$$

Expanding Eq. (15) results in

$$\begin{aligned} \dot{V} &= c\alpha c\beta(X + G_x + T_x) + s\beta(Y + G_y + T_y) \\ &\quad + s\alpha c\beta(Z + G_z + T_z) \\ \dot{\alpha} &= (1/Vc\beta)[-s\alpha(G_x + X + T_x) + c\alpha(G_z + Z + T_z)] \\ &\quad + q - [pc\alpha + rs\alpha]\tan(\beta) \\ \dot{\beta} &= (1/V)[-c\alpha s\beta(G_x + X + T_x) + c\beta(G_y + Y + T_y) \\ &\quad - s\alpha s\beta(G_z + Z + T_z)] + ps\alpha - rc\alpha \end{aligned} \tag{16}$$

Acceleration Dynamics

This section derives rigid-body differential equations for the body axis accelerations at the c.g. The body axis acceleration at the c.g. is given by

$$\begin{bmatrix} A_x \\ A_y \\ A_z \end{bmatrix} = \begin{bmatrix} X + G_x + T_x \\ Y + G_y + T_y \\ Z + G_z + T_z \end{bmatrix} \tag{17}$$

Expanding these terms gives

$$\begin{bmatrix} A_x \\ A_y \\ A_z \end{bmatrix} = \left\{ \begin{bmatrix} \dfrac{\bar{q}S}{m} C_x(\alpha, \beta, \delta_e, \delta_a, \delta_r) \\ \dfrac{\bar{q}S}{m} C_y(\alpha, \beta, \delta_e, \delta_a, \delta_r) \\ \dfrac{\bar{q}S}{m} C_z(\alpha, \beta, \delta_e, \delta_a, \delta_r) \end{bmatrix} + \begin{bmatrix} G_x \\ G_y \\ G_z \end{bmatrix} + \begin{bmatrix} T_x \\ T_y \\ T_z \end{bmatrix} \right\} \tag{18}$$

where the functional dependence of the aerodynamics on α, β, and the aerodynamic control surfaces δ_i is shown to highlight what terms will be differentiated. The aerodynamic effects due to the body rates p, q, and r and the plunge effects from $\dot{\alpha}$ and $\dot{\beta}$ are assumed zero. If these effects are known, then they should be included. Differentiating this expression yields

$$\begin{bmatrix}\dot{A}_x\\ \dot{A}_y\\ \dot{A}_z\end{bmatrix} = \frac{2\bar{q}S}{mV}\begin{bmatrix}C_x\\ C_y\\ C_z\end{bmatrix}\dot{V} + \frac{\bar{q}S}{m}\begin{bmatrix}C_{x_\alpha}\\ C_{y_\alpha}\\ C_{z_\alpha}\end{bmatrix}\dot{\alpha} + \frac{\bar{q}S}{m}\begin{bmatrix}C_{x_\beta}\\ C_{y_\beta}\\ C_{z_\beta}\end{bmatrix}\dot{\beta}$$

$$+\frac{\bar{q}S}{m}\begin{bmatrix}C_{x_{\delta e}} & C_{x_{\delta a}} & C_{x_{\delta r}}\\ C_{y_{\delta e}} & C_{y_{\delta a}} & C_{y_{\delta r}}\\ C_{z_{\delta e}} & C_{z_{\delta a}} & C_{z_{\delta r}}\end{bmatrix}\begin{bmatrix}\dot{\delta}_e\\ \dot{\delta}_a\\ \dot{\delta}_r\end{bmatrix} + \begin{bmatrix}\dot{G}_x + \dot{T}_x\\ \dot{G}_y + \dot{T}_y\\ \dot{G}_z + \dot{T}_z\end{bmatrix} \tag{19}$$

where the subscripts denote partial derivatives. Grouping terms results in

$$\begin{bmatrix}\dot{A}_x\\ \dot{A}_y\\ \dot{A}_z\end{bmatrix} = \frac{\bar{q}S}{mV}\begin{bmatrix}2C_x & C_{x_\alpha} & C_{x_\beta}\\ 2C_y & C_{y_\alpha} & C_{y_\beta}\\ 2C_z & C_{z_\alpha} & C_{z_\beta}\end{bmatrix}\begin{bmatrix}\dot{V}\\ V\dot{\alpha}\\ V\dot{\beta}\end{bmatrix}$$

$$+\frac{\bar{q}S}{m}\begin{bmatrix}C_{x_{\delta e}} & C_{x_{\delta a}} & C_{x_{\delta r}}\\ C_{y_{\delta e}} & C_{y_{\delta a}} & C_{y_{\delta r}}\\ C_{z_{\delta e}} & C_{z_{\delta a}} & C_{z_{\delta r}}\end{bmatrix}\begin{bmatrix}\dot{\delta}_e\\ \dot{\delta}_a\\ \dot{\delta}_r\end{bmatrix} + \begin{bmatrix}\dot{G}_x + \dot{T}_x\\ \dot{G}_y + \dot{T}_y\\ \dot{G}_z + \dot{T}_z\end{bmatrix} \tag{20}$$

Substituting from Eq. (14) yields

$$\begin{bmatrix}\dot{A}_x\\ \dot{A}_y\\ \dot{A}_z\end{bmatrix} = \begin{bmatrix}\dot{G}_x + \dot{T}_x\\ \dot{G}_y + \dot{T}_y\\ \dot{G}_z + \dot{T}_z\end{bmatrix} + \begin{bmatrix}X_{\delta e} & X_{\delta a} & X_{\delta r}\\ Y_{\delta e} & Y_{\delta a} & Y_{\delta r}\\ Z_{\delta e} & Z_{\delta a} & Z_{\delta r}\end{bmatrix}\begin{bmatrix}\dot{\delta}_e\\ \dot{\delta}_a\\ \dot{\delta}_r\end{bmatrix}$$

$$+\frac{1}{V}\begin{bmatrix}2X & X_\alpha & X_\beta\\ 2Y & Y_\alpha & Y_\beta\\ 2Z & Z_\alpha & Z_\beta\end{bmatrix}\begin{bmatrix}c\alpha c\beta & s\beta & s\alpha c\beta\\ -s\alpha/c\beta & 0 & c\alpha/c\beta\\ c\alpha s\beta & c\beta & -s\alpha s\beta\end{bmatrix}\begin{bmatrix}\dot{u}\\ \dot{v}\\ \dot{w}\end{bmatrix} \tag{21}$$

Substituting for $[\dot{u} \;\; \dot{v} \;\; \dot{w}]^T$ yields

$$\begin{bmatrix}\dot{A}_x\\ \dot{A}_y\\ \dot{A}_z\end{bmatrix} = \begin{bmatrix}\dot{G}_x + \dot{T}_x\\ \dot{G}_y + \dot{T}_y\\ \dot{G}_z + \dot{T}_z\end{bmatrix} + \begin{bmatrix}X_{\delta e} & X_{\delta a} & X_{\delta r}\\ Y_{\delta e} & Y_{\delta a} & Y_{\delta r}\\ Z_{\delta e} & Z_{\delta a} & Z_{\delta r}\end{bmatrix}\begin{bmatrix}\dot{\delta}_e\\ \dot{\delta}_a\\ \dot{\delta}_r\end{bmatrix}$$

$$+\frac{1}{V}\begin{bmatrix}2X & X_\alpha & X_\beta\\ 2Y & Y_\alpha & Y_\beta\\ 2Z & Z_\alpha & Z_\beta\end{bmatrix}W(\alpha, \beta)$$

$$\times\left\{\begin{bmatrix}A_x\\ A_y\\ A_z\end{bmatrix} + V\begin{bmatrix}s\beta r - s\alpha c\beta q\\ s\alpha c\beta p - c\alpha c\beta r\\ c\alpha c\beta q - s\beta p\end{bmatrix}\right\} \tag{22}$$

Note that the time rates of change of the accelerations are modeled proportional to actuator rates. Thus, an actuator dynamics model is required to model the accelerations as states in a state space model.

Autopilot Design Models

Maximizing overall missile performance requires choosing the appropriate autopilot command structure for each mission phase. This may include designing a different autopilot for separation during launch, an agile turn at high AOA, midcourse where a long flyout is required, and endgame where terminal homing maneuvers are necessary. The autopilot can command either body rates, wind angles, attitudes, or accelerations.

During launch a body rate command system is typically used. Rate command autopilots are very robust to the uncertain proximity aerodynamics. During an agile turn, directional control of the missile's velocity vector relative to the missile body is desired. This equates to commanding AOA or sideslip and regulating roll to zero. During midcourse and in the terminal phase, an acceleration command autopilot is typically used. At the end of terminal homing, during a guidance integrated fuse maneuver, the missile attitude may be commanded to improve the lethality of the warhead.

Separation, midcourse, and endgame autopilots have been designed and implemented in production missiles and are in general well understood. Autopilot designs for high-AOA flight are significantly less understood. Missile performance during the agile turn can be maximized by maximizing the missile's turn rate. High missile turn rates lead to faster target intercepts. The missile's turn rate (for a pitch-plane maneuver) is given by

$$\dot{\gamma} = \frac{A_z\cos(\alpha) - A_x\sin(\alpha)}{V} \tag{23}$$

High turn rates can be achieved by commanding a constant high AOA or by commanding large values of normal acceleration $[A_z\cos(\alpha) - A_x\sin(\alpha)]$. Simulation studies have shown that due to the large changes in the missile's velocity (V) at high AOAs (due to the high drag), commanding body accelerations during an agile turn may not be desirable.

The nonlinear missile dynamics can be written as

$$\dot{\boldsymbol{x}} = f(\boldsymbol{x}, \boldsymbol{u}) \tag{24}$$

To form a linear model, partial derivatives of f_i are needed with respect to each state variable and each control input. These partial derivatives are evaluated at a specific flight condition design point. This would typically be at a trimmed equilibrium condition; however, at high AOAs the missile is generally not in what is considered an equilibrium condition.

Pitch Autopilot Design Model

The pitch-plane nonlinear AOA and pitch rate dynamics are described in Eqs. (1) and (16). Zeroing roll-yaw dynamics and linearizing about α_0 result in

$$\dot{\alpha} = (Z_\alpha/V)\alpha + q + (Z_\delta/V)\delta_e - (s\alpha_0/V)T_x + (c\alpha_0/V)T_z$$

$$\dot{q} = M_\alpha\alpha + M_q q + M_\delta\delta_e + M_T \tag{25}$$

where

$$Z_\alpha = \frac{\partial\dot{\alpha}}{\partial\alpha} = \left\{\left(\frac{\partial Z}{\partial\alpha} - G_x - T_x - X\right)c\alpha - \left(\frac{\partial X}{\partial\alpha} + G_z + T_z + Z\right)s\alpha\right\}_{\alpha=\alpha_0}$$

$$Z_\delta = \frac{\partial\dot{\alpha}}{\partial\delta_e} = \left\{\frac{\partial Z}{\partial\delta_e}c\alpha - \frac{\partial X}{\partial\delta_e}s\alpha\right\}_{\alpha=\alpha_0}$$

$$M_\alpha = \left.\frac{\partial M}{\partial\alpha}\right|_{\alpha=\alpha_0}, \qquad M_q = \left.\frac{\partial M}{\partial q}\right|_{\alpha=\alpha_0}, \qquad M_\delta = \left.\frac{\partial M}{\partial\delta_e}\right|_{\alpha=\alpha_0}$$

Because most TVC actuators are limited to small deflection angles, the $\sin(\delta_{T_e}) \approx \delta_{T_e}$, and $\cos(\delta_{T_e}) \approx 1$, resulting in

$$T_x = T/m, \qquad T_z = -(T/m)\delta_{T_e}, \qquad M_T = -(l_T T/I_{yy})\delta_{T_e} \tag{26}$$

To model RCS thruster forces (axial thrust T is due to main engine) [see Eqs. (7) and (9)]

$$T_x = T/m, \qquad T_z = T_{\mathrm{RCS}}/m, \qquad M_T = -(l_T/I_{yy})T_{\mathrm{RCS}} \tag{27}$$

Neglecting the influence of gravity on the AOA dynamics (because it is divided by V) and the $T\sin(\alpha_0)$ term (because it represents a constant) and combining these into a linear matrix model result in

$$\begin{bmatrix}\dot{\alpha}\\ \dot{q}\end{bmatrix} = \begin{bmatrix}\dfrac{Z_\alpha}{V} & 1\\ M_\alpha & M_q\end{bmatrix}\begin{bmatrix}\alpha\\ q\end{bmatrix} + \begin{bmatrix}\dfrac{Z_\delta}{V}\\ M_\delta\end{bmatrix}\delta_e$$

$$+\begin{bmatrix}\dfrac{c\alpha_0}{mV}\\ \dfrac{l_T}{I_{yy}}\end{bmatrix}T_{\mathrm{RCS}} + \begin{bmatrix}\dfrac{T\left(s\alpha_0 s\delta_{T_0} - c\alpha_0 c\delta_{T_0}\right)}{mV}\\ \dfrac{-Tl_T}{I_{yy}}\end{bmatrix}\delta_{T_e} \tag{28}$$

This state-space model can be used to design pitch autopilots at a specific flight condition (α_0, Mach, altitude, c.g.). If A_z rather than α is preferred as a state variable, then replace the $\dot{\alpha}$ equation with $\dot{A}_z$ from Eq. (22). This also requires removing α from the pitch rate dynamics and adding an actuator model to include the terms proportional to the actuator deflection rates.

Roll-Yaw Autopilot Design Model

The lateral directional nonlinear dynamics are described in Eqs. (1) and (16). Zeroing the pitch dynamics and linearizing about α_0 (with $\beta = 0$) result in

$$\begin{bmatrix} \dot{\beta} \\ \dot{p} \\ \dot{r} \end{bmatrix} = \begin{bmatrix} Y_\beta/V & s\alpha_0 + (Y_p/V) & c\alpha_0 + (Y_r/V) \\ L_\beta & L_p & L_r \\ N_\beta & N_p & N_r \end{bmatrix} \begin{bmatrix} \beta \\ p \\ r \end{bmatrix} + \begin{bmatrix} Y_{\delta a}/V & Y_{\delta r}/V \\ L_{\delta a} & L_{\delta r} \\ N_{\delta a} & N_{\delta r} \end{bmatrix} \begin{bmatrix} \delta_a \\ \delta_r \end{bmatrix} + \begin{bmatrix} 1/V & 0 & 0 \\ 0 & 1 & 0 \\ 0 & 0 & 1 \end{bmatrix} \begin{bmatrix} T_y \\ L_T \\ N_T \end{bmatrix} \tag{29}$$

where the elements of the matrices were obtained in a similar manner to Eq. (25).

For TVC (assuming a small TVC angle δ_{Tr}) results in

$$T_y = \frac{-T}{m}\delta_{Tr}, \qquad L_T = \frac{-l_T I_{xz} T}{I_{xx} I_{zz} - I_{xz}^2}\delta_{Tr}$$
$$N_T = \frac{-l_T I_{xx} T}{I_{xx} I_{zz} - I_{xz}^2}\delta_{Tr} \tag{30}$$

Modeling an RCS control system yields

$$T_y = \frac{\bar{T}_y}{m}, \qquad L_T = \frac{l_{\text{Roll}} \bar{T}_{\text{Roll}}}{I_{xx}} + \frac{l_T I_{xz} \bar{T}_y}{I_{xx} I_{zz} - I_{xz}^2}$$
$$N_T = \frac{l_T I_{xx} \bar{T}_y}{I_{xx} I_{zz} - I_{xz}^2} \tag{31}$$

Neglecting gravity results in the following linear autopilot design model:

$$\begin{bmatrix} \dot{\beta} \\ \dot{p} \\ \dot{r} \end{bmatrix} = \begin{bmatrix} \frac{Y_\beta}{V} & s\alpha_0 + \frac{Y_p}{V} & c\alpha_0 + \frac{Y_r}{V} \\ L_\beta & L_p & L_r \\ N_\beta & N_p & N_r \end{bmatrix} \begin{bmatrix} \beta \\ p \\ r \end{bmatrix} + \begin{bmatrix} \frac{-T}{m} \\ \frac{-l_T I_{xz} T}{I_{xx} I_{zz} - I_{xz}^2} \\ \frac{-l_T I_{xx} T}{I_{xx} I_{zz} - I_{xz}^2} \end{bmatrix} \delta_{Tr}$$
$$+ \begin{bmatrix} \frac{Y_{\delta a}}{V} & \frac{Y_{\delta r}}{V} \\ L_{\delta a} & L_{\delta r} \\ N_{\delta a} & N_{\delta r} \end{bmatrix} \begin{bmatrix} \delta_a \\ \delta_r \end{bmatrix} + \begin{bmatrix} \frac{1}{m} & 0 \\ \frac{l_T I_{xz}}{I_{xx} I_{zz} - I_{xz}^2} & \frac{l_{\text{Roll}}}{I_{xx}} \\ \frac{l_T I_{xx}}{I_{xx} I_{zz} - I_{xz}^2} & 0 \end{bmatrix} \begin{bmatrix} \bar{T}_y \\ \bar{T}_{\text{Roll}} \end{bmatrix} \tag{32}$$

This state-space model can be used to design roll-yaw autopilots at a specific flight condition (α_0, Mach, altitude, c.g.). Note that β was assumed to be zero for a bank-to-turn missile. This modeling assumption is used because at high AOAs β must be kept very small to keep from saturating the roll channel controls.

Sensor Measurements

Most tactical missiles use strapdown inertial measurement units (IMU) for navigation, which have three accelerometers and three gyros. The accelerometers and gyros are arranged into a triad to measure accelerations along and rotational rates about the x, y, and z body axes, respectively. Because of packaging considerations, the IMU is usually not located at the missile's c.g.

The location of the accelerometers relative to the c.g. greatly affects the measured accelerations and must be accounted for in the design of the flight control system. Ideally, if the accelerometers are located at the c.g., then they measure just the translational accelerations. If the accelerometers are located off the c.g., then they measure a combination of translational accelerations and rotational accelerations. This can be expressed as

$$a_{\text{IMU}} = a_{\text{c.g.}} + \dot{\omega} \times \boldsymbol{r}_{\text{IMU}} + \omega \times \omega \times \boldsymbol{r}_{\text{IMU}} \tag{33}$$

where $\boldsymbol{r}_{\text{IMU}}$ is a vector from the c.g. to the IMU and $\omega = [p \;\; q \;\; r]^T$. Note that the sensed accelerations are a nonlinear function of the body rates.

Linear sensor models are required for linear autopilot design. On symmetric airframes the y and z axis c.g. offsets are usually small and can be neglected. The z-axis accelerometer is compensated for the x-axis c.g. offset as follows:

$$Az_{\text{IMU}} = Az_{\text{c.g.}} + (x_{\text{c.g.}} - x_{\text{IMU}})\dot{q} \tag{34}$$

This effect can have a dramatic impact on the flight control system design. Equation (34) shows that the rotational dynamics are blended with the translational dynamics. This changes the zeros of the transfer function from the control input to the sensor output.

Consider the transfer function from elevator δ_e to acceleration $Az_{\text{c.g.}}$ [from Ref. 4, Eq. (4)] given by

$$\frac{Az_{\text{c.g.}}}{\delta_e} = \frac{\omega_a^2\left(Z_{\delta e}s^2 + Z_\alpha M_{\delta e} - Z_{\delta e} M_\alpha\right)}{\left[s^2 - (Z_\alpha/V)s - M_\alpha\right]\left(s^2 + 2\zeta_a\omega_a s + \omega_a^2\right)} \tag{35}$$

For tail-controlled missiles this transfer function is nonminimum phase [has a right half-plane (RHP) zero]. As the elevator δ_e deflects, the fin force ($Z_{\delta e}\delta_e$) accelerates the missile in the wrong direction. However, this fin force creates a pitching moment that rotates the missile. As the missile rotates, the body force builds ($Z_\alpha \alpha$), accelerating the missile in the correct (commanded) direction. Aerodynamically unstable ($M_\alpha > 0$) tail-controlled missiles pose a considerable control challenge in that they have both RHP poles and zeros.

The transfer function from δ_e to Az_{IMU} does not have the same zeros as using $Az_{\text{c.g.}}$. Figure 7 illustrates the location of the acceleration zeros as the sensor is moved along the body of the missile. When the IMU is aft of the c.g., the two zeros are real with one in the RHP. As the IMU moves forward of the c.g. to the center of percussion,[5] the zeros bifurcate and become complex, moving in along the $j\omega$ axis.

The autopilot designer can shape the zeros in the acceleration transfer function by placing the sensor at a different location. Depending upon how the feedback gains are designed, this can be exploited to improve stability and transient performance. See Hsu and Robel,[6] and the references therein, for more discussion on zeros and their impact on the flight control system.

Fin Actuator Model

There are four tail fins each driven by an electromechanical (EM) actuator. The fin actuator dynamics can be modeled with a second-order transfer function. The significant nonlinearities typically modeled include position and rate limits as well as mechanical backlash.

The fin mixing logic that relates δ_e, δ_a, and δ_r commands to individual fin deflections is configuration specific and depends upon whether the missile is flown with an "×" or "+" tail. Here (for an × tail) the equations for the fin mixing logic are

$$\begin{bmatrix} \delta_1 \\ \delta_2 \\ \delta_3 \\ \delta_4 \end{bmatrix} = \begin{bmatrix} 1 & -1 & -1 \\ 1 & -1 & 1 \\ 1 & 1 & -1 \\ 1 & 1 & 1 \end{bmatrix} \begin{bmatrix} \delta_e \\ \delta_a \\ \delta_r \end{bmatrix} \tag{36}$$

where δ_e, δ_a, and δ_r are the autopilot pitch, roll, and yaw fin commands, respectively, distributed to the four fins, and the δ_i, $i = 1, \ldots, 4$, are the actual fin deflections. Note that it is the δ_i that exhibit the nonlinearities (fin and rate limits and backlash).

RCS Thruster Actuator Model

RCS actuators can be built with EM valves, hot gas poppet valves, hydraulic valves, and solenoid valves. They can be stand-alone systems (requiring their own propellant) or can be integrated with the main engine (bleed off the main engine chamber pressure). They can also be on–off or continuous (throttling).

Both the continuous and on–off RCS actuators can be modeled with a first-order transfer function. The 63% rise time of the thrust is used to specify the time constant in the transfer function. The RCS thrust is magnitude and rate limited. In addition, some on–off designs cannot change states (on or off) until they are fully opened or closed.

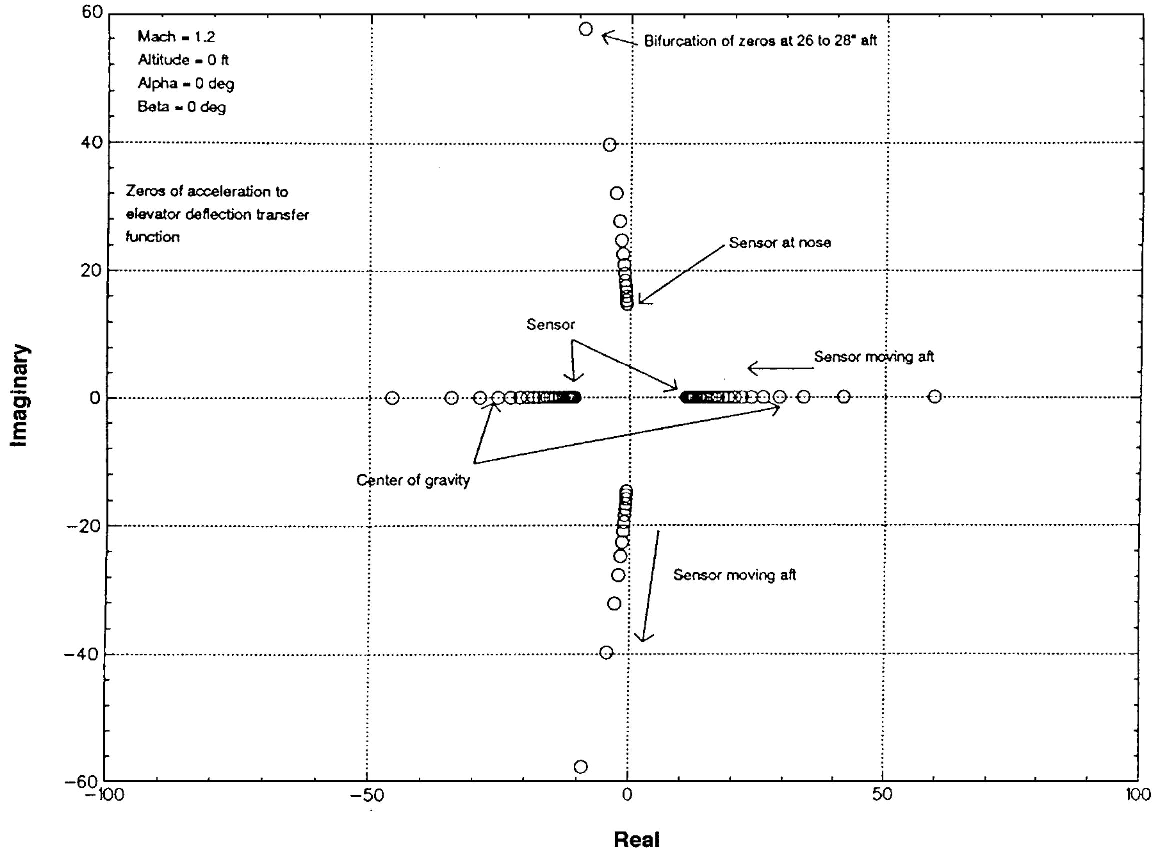

Fig. 7 Acceleration zeros root locus vs sensor location.

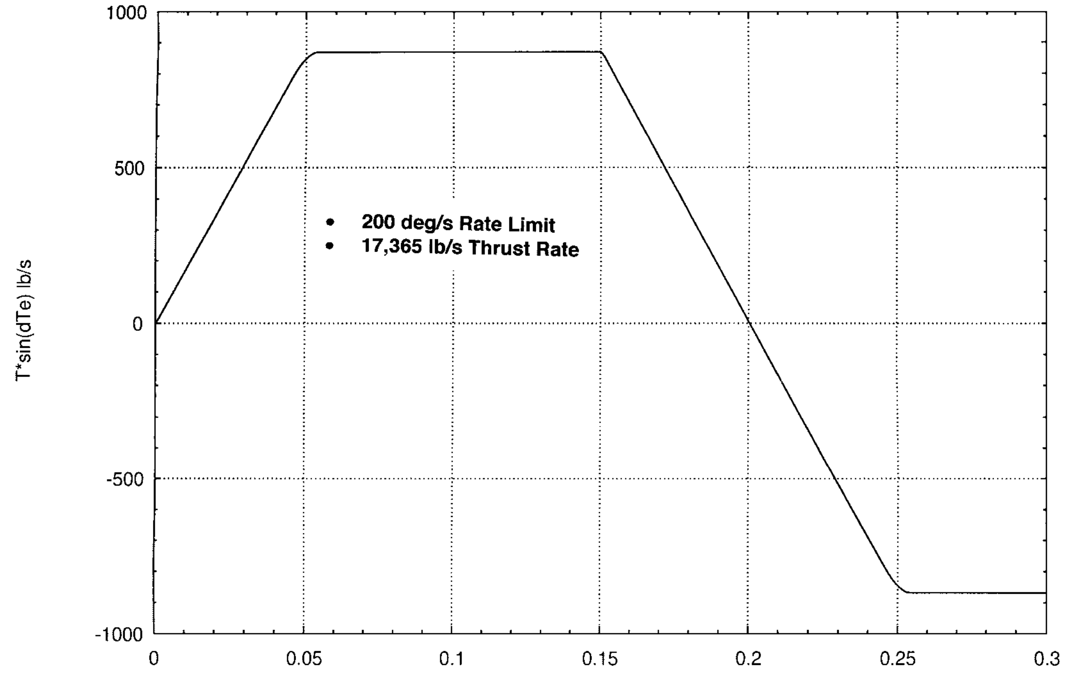

Fig. 8 TVC normal thrust from a rate and position limited actuator response to a 10-deg square wave input.

TVC Actuator Model

TVC actuators operate in a similar manner to the fin actuators and are usually modeled with second-order transfer functions. The nonlinearities typically modeled include position and rate limits as well as mechanical backlash.

Figure 8 shows a plot of the normal thrust produced by a nonlinear TVC actuator response (no backlash modeled) to a 10-deg square wave input. This response illustrates the effects of both the position and rate limiting. For a 5000-lbf main engine motor and a deflection limit of 10 deg, the maximum normal force is 868.24 lbf.

Using the response shown in the Figure 8, the maximum thrust rate for the TVC actuator can be computed as a function of the TVC nozzle rate limit. A fast thrust rate is required to maintain stability and to capture the high-AOA command during the agile turn.

Figure 9 shows a comparison of the TVC thrust rate capability with that of a 500-lbf RCS jet, in which the RCS jet is parameterized by the time it takes the jet to reach full thrust.

For a 200-deg/s TVC actuator rate limit the thrust rate is slightly less than 20,000 lbf/s. This equates to a 500-lbf RCS jet that reaches its full thrust in 34.7 ms. At a 400 deg/s TVC rate limit, the equivalent

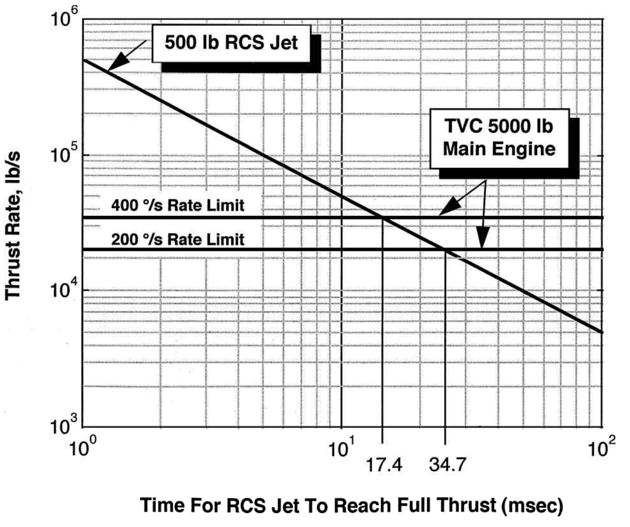

Fig. 9 TVC and thruster thrust rate capabilities.

RCS jet time to full thrust is 17.4 ms. This figure indicates that the TVC actuator system is somewhat slower than the RCS system in developing normal thrust. High TVC rates will be required for the TVC actuator to slew the thrust vector to its maximum position. These high TVC rates will in turn drive the TVC power consumption and battery sizing requirements upward, thus increasing the cost and weight of the missile.

Flexible-Body Dynamics

In deriving the autopilot design models it was assumed that the missile was a rigid body. In fact, it is a flexible body, and these dynamics have a significant impact on the sensed accelerations and body rates. The discussion here is limited to the airframe's pitch plane. Also discussed is the tail-wags-the-dog effect due to fin mass unbalance and inertia and TVC nozzle inertia. Reference 2 contains details on modeling these dynamics.

Consider the following flexible model:

$$\begin{bmatrix} \dot\alpha \\ \dot q \\ \dot b_1 \\ \ddot b_1 \end{bmatrix} = \begin{bmatrix} Z_\alpha/V & 1 & Z_{b1} & Z_{\dot b 1} \\ M_\alpha & M_q & M_{b1} & M_{\dot b 1} \\ 0 & 0 & 0 & 1 \\ b_{\alpha 1} & b_{q1} & b_{b1} & b_{\dot b 1} \end{bmatrix} \begin{bmatrix} \alpha \\ q \\ b_1 \\ \dot b_1 \end{bmatrix} + \begin{bmatrix} Z_\delta/V & Z_{\ddot\delta}/V \\ M_\delta & M_{\ddot\delta} \\ 0 & 0 \\ b_{\delta 1} & b_{\ddot\delta 1} \end{bmatrix} \begin{bmatrix} \delta_e \\ \ddot\delta_e \end{bmatrix} \tag{37}$$

This linear analysis model describes the pitch-plane rigid-body dynamics (α, q) combined with the first bending mode (b_1), including the tail-wags-the-dog effects proportional to $\ddot\delta_e$.

The pitch rate gyro and z-axis accelerometer measurements are

$$q_{\text{FLEX}} = q_{\text{IMU}} + F'_{A1}\dot b_1, \qquad Az_{\text{FLEX}} = Az_{\text{IMU}} + F_{A1}\ddot b_1/g \tag{38}$$

Partitioning the A matrix in Eq. (37) into 2×2 blocks, the (1, 1) block is the same as in Eq. (28) and describes the rigid-body dynamics. The (1, 2) block describes the changes in the aerodynamic forces and moments due to the body flexure. The (2, 1) block describes how the rigid-body states (α, q) excite the bending mode. The (2, 2) block describes the first bending mode's second-order dynamics.

In addition to the rigid-body states (α, q), the fin deflection δ_e also excites the bending dynamics. Assuming the fin c.g. is located off the fin's rotational axis, when the fin rotates, a bending torque is applied to the missile body that is proportional to both the fin's inertia and any mass unbalance. This effect is called the *tail-wags-the-dog effect* and can be significant. When TVC is used, this effect is large because the nozzle is heavy and its c.g. is not located about its rotational axis.

The IMU sensor measurements are corrupted by the flexible dynamics. Filters are designed to remove these signals from the sensed rates and accelerations. Unfortunately, these filters add gain attenuation and phase lag at the loop gain crossover frequency, thus impacting stability margins.

Control Power Analysis

The autopilot design models can be used to assess the control effector's capability to control the missile's dynamics as the flight envelope changes. This section presents a static control power analysis of the missile's pitch dynamics, examining for what part of the flight envelope the aero, RCS, and TVC control effectors are the most useful.

Aero control effectors depend upon dynamic pressure to generate control power. At low velocities aero control effectors have low control power. The aero control effectors also depend upon the AOA and lose effectiveness at high AOAs.

Assuming that jet interaction effects are neglected, RCS thrusters provide a fixed level of thrust normal to the x-body axis independent of flight condition. The same level of control power is obtained at low and high velocities.

Thrust vector control exhibits characteristics independent of flight condition the same as RCS control. TVC actuators have a limited deflection that then limits the normal thrust. Control power data for the TVC designs are not presented, but the same trends apply to both the TVC and RCS control effectors.

A state space model for the missile's dynamics can be written as $\dot x = Ax + Bu$, where the aero and RCS control inputs enter into the dynamics through the B matrix. The B matrix can be partitioned as $B = [B_\delta \;\; B_{\text{RCS}}]$. The control effectiveness, or control power, can be analyzed by computing the size of the B matrix as a function of AOA, c.g. location, altitude, and Mach number. The singular values of the B matrix are computed,[7] and the maximum singular value is examined as the flight envelope parameters vary.

To minimize the amount of propellant used to perform maneuvers, it is important to know at what velocities and AOAs the aero controls are effective. Similarly, for RCS and TVC controls, it is important to know at what flight conditions the main engine must be providing thrust.

Study results show that the tail fins are very effective near zero AOA but lose their pitch moment capability as the AOA increases or as the velocity decreases, decreasing the dynamic pressure. Assuming that jet interaction effects are neglected, the RCS jet's pitch moment capability is constant with AOA and Mach number. At low Mach numbers the RCS control is more effective than aero control. At high Mach numbers, the aero controls are much more effective than the RCS jets. As altitude increases, the aero becomes less effective and requires an increase in velocity to maintain its effectiveness. This is due to the decrease in dynamic pressure as altitude increases.

Figure 10 summarizes data comparing missile fin and RCS control effectiveness for an empty weight configuration. The RCS control

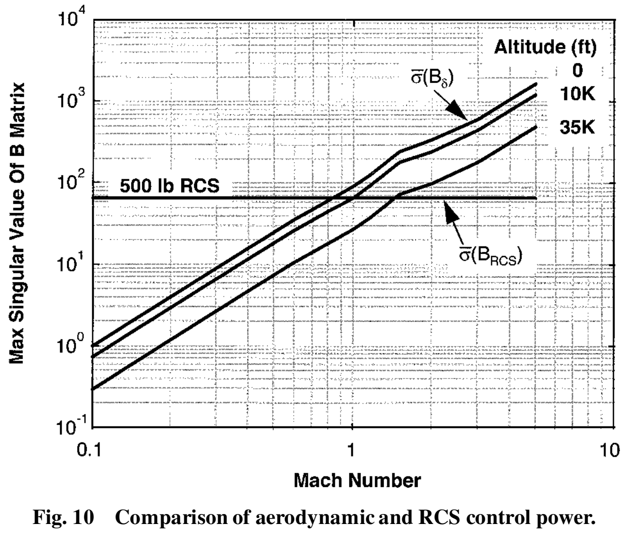

Fig. 10 Comparison of aerodynamic and RCS control power.

has a fixed magnitude vs Mach number. The three curves that change magnitude with Mach number represent the amount of aero control power for 0-, 10,000-, and 35,000-ft altitudes. For small AOAs and above Mach 0.8, the fins are as effective as the RCS controls (data are for 0-deg AOA). As expected, at the higher Mach numbers, the aero control is significantly more effective than the RCS control.

Guidance and Control

Nonlinear guidance and control are used to intercept targets. During agile maneuvers, guidance commands are computed to maneuver the missile until the target is in the seeker's field of view and locked on. After lock on, the guidance uses augmented proportional navigation to steer the missile through terminal homing and intercept.

Autopilots were designed using linear quadratic regulator techniques from Ref. 8 to produce a gain scheduled autopilot. The autopilot used integral error control to track guidance commands. Simulation results are presented for a missile using RCS thrusters and small aerodynamic fins. This missile configuration included small nose strakes to mitigate phantom yaw effects, as shown in Figs. 3 and 4.

During the agile turn, missile roll attitude and AOA are controlled by the autopilot, with sideslip angle regulated to zero. During this phase the missile flies in a preferred orientation mode similar to bank-to-turn control. After the agile turn, the autopilot is reconfigured to control body accelerations in a standard skid-to-turn mode. Bank-to-turn control at high AOA is used to prevent asymmetries from saturating the roll control channel. Also, the aerodynamic fins are commanded to a fixed position at zero. This is done to reduce the roll control requirements and because of unpredictable sign reversals in the aerodynamic fin control derivatives.

Figure 11 displays six-degree-of-freedom simulation time histories of an agile missile intercepting a target in the rear hemisphere. A merge scenario was simulated with both aircraft at Mach 0.8 and the target initially displaced by 1500 ft in crosstrack and downtrack. This merge scenario represents only one of many scenarios that must be used to evaluate the missile's performance. A 90-deg AOA command was used to turn the missile into the rear hemisphere, and then after seeker acquisition of the target, proportional navigation is used to intercept the target. Asymmetric vortex shedding was simulated during the flyout.

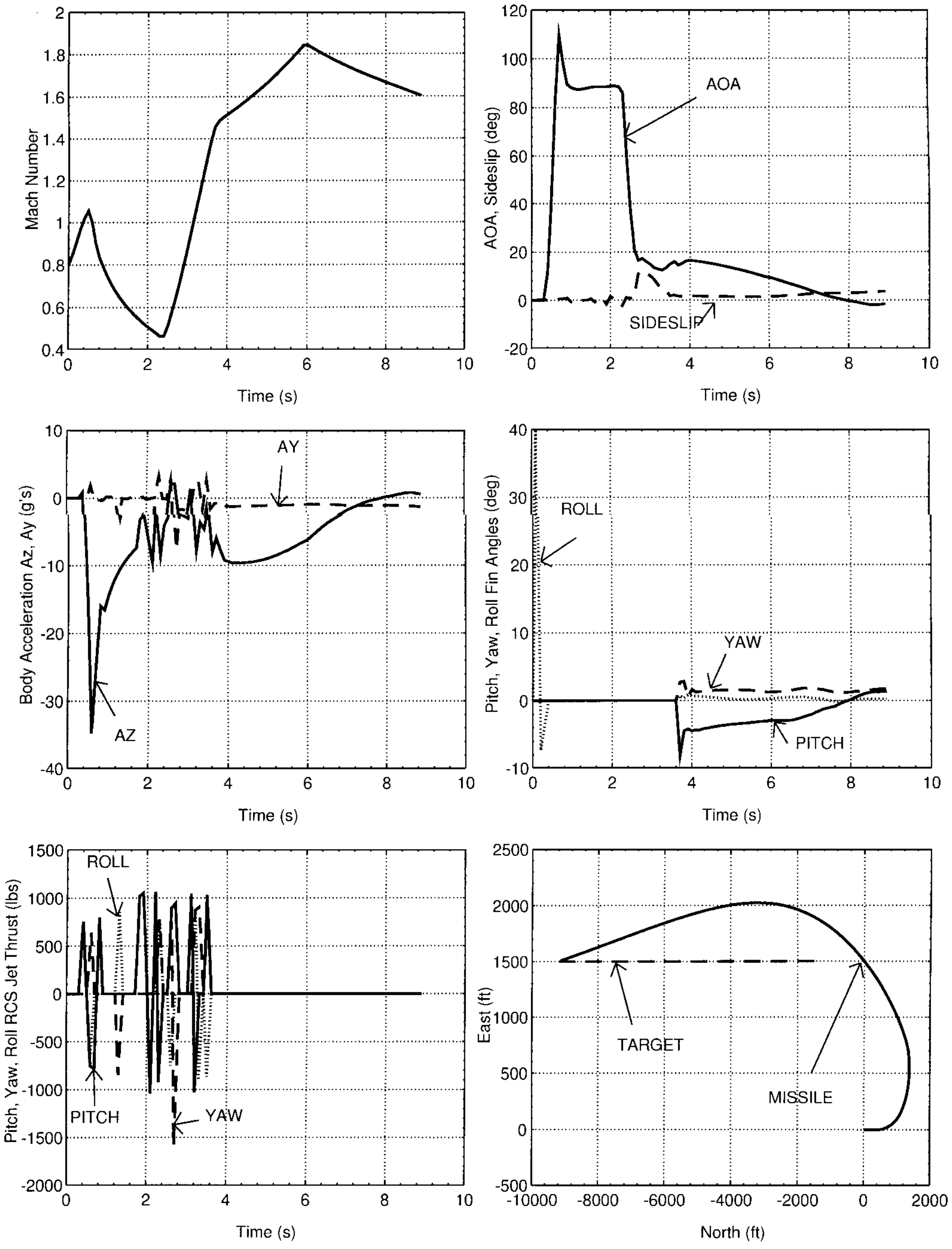

Fig. 11 Agile missile six-degree-of-freedom simulation time histories.

The Mach number time history shown in Fig. 11 demonstrates how quickly the missile loses velocity while at high AOA. Following launch, aerodynamic controls are used to provide a safe separation from the aircraft and roll the missile to a preferred maneuver plane. Then RCS thrusters are used to perform the high-AOA maneuver with the fins commanded to zero. After the turn, the missile switches back to aerodynamic control. This switch is based upon missile speed knowing when the fins are aerodynamically effective. During the remainder of the simulation the missile flies using only fin control.

The simulation models an RCS system that is integrated with the main propulsion system, in that the thrusters bleed off the main engine pressure chamber. RCS control is used only until the velocity increases to where the fins are effective. This strategy minimizes the amount of propellant used for flight control, thus maximizing the penetration into the rear hemisphere.

Conclusions

Several key technological challenges for agile missile flight were discussed. These challenges include asymmetric vortex shedding, missile stability variations, roll control at high angles of attack, jet interaction effects, and nonlinear guidance and control. During high-angle-of-attack flight, the missile flies in a preferred orientation to prevent roll saturation and to mitigate aerodynamic uncertainties caused by phantom yaw and fin sign reversals. Nonlinear simulation results with asymmetric vortex shedding show a low thruster activity used to maintain stability and track guidance commands.

References

[1] McRuer, D., Ashkenas, I., and Graham, D., *Aircraft Dynamics and Automatic Control*, Princeton Univ. Press, Princeton, NJ, 1973, pp. 203–262.

[2] Blakelock, J. H., *Automatic Control of Aircraft and Missiles*, Wiley, New York, 1991, Chaps. 1–3.

[3] Wassom, S. R., Faupell, L. C., and Perley, T., "Integrated Aerofin/TVC for Tactical Missiles," *Journal of Propulsion and Power*, Vol. 7, No. 3, 1991, pp. 374–381.

[4] Wise, K. A., "Comparison of Six Robustness Tests Evaluating Missile Autopilot Robustness to Uncertain Aerodynamics," *Journal of Guidance, Control, and Dynamics*, Vol. 15, No. 4, 1992, pp. 861–870.

[5] Meriam, J. L., *Dynamics*, Wiley, New York, 1991, p. 244.

[6] Hsu, C. S., and Robel, G., "Zeros and Transmission Zeros of Flight Control Systems," *AIAA Guidance, Navigation, and Control Conference*, AIAA, New York, 1987 (AIAA Paper 87-2237).

[7] Douglas, R., Mackler, S., and Speyer, J., "Robust Hover Control for a Short Takeoff/Vertical Landing Aircraft," *Proceedings of the AIAA Guidance, Navigation, and Control Conference*, AIAA, Washington, DC, 1990, pp. 150–163.

[8] Wise, K. A., "Bank-to-Turn Missile Autopilot Design Using Loop Transfer Recovery," *Journal of Guidance, Control, and Dynamics*, Vol. 13, No. 1, 1990, pp. 145–152.